# Investigation of the 30P30N Slat Flow Field with Passive Control Devices Using Particle Image Velocimetry

Yang Zhang,* Ross Richardson, † and Louis N. Cattafesta III‡
*Florida Center for Advanced Aero-Propulsion (FCAAP), Florida A&M University and Florida State University, Tallahassee, Florida, 32310*

Meelan M. Choudhari,§ Kyle A. Pascioni,¶ Mehdi R. Khorrami,‖ David P. Lockard,** and Travis Turner††
*NASA Langley Research Center, Hampton, VA, 23681*

**The leading-edge slat of a high-lift wing is one of the main noise contributors during approach and landing. This paper describes an experimental investigation of the velocity field associated with multiple passive noise treatments, including slat-cusp extensions, a cove filler, and a gap filler, on a two-dimensional multielement high-lift 30P30N airfoil. Previous work documented comparisons of both surface and far field pressure fluctuations in the presence of these devices with those for a baseline case at different flow conditions. However, important information related to the velocity fields was missing from the previous measurements, hindering the ability to elucidate changes in the flow physics associated with the noise treatments. Therefore, two-component Particle Image Velocity has been used to investigate the influence of passive noise treatments on the flow fields. All measurements are taken at an effective, free-air angle of attack of $5.5^\circ$ and a stowed-chord-based Reynolds number of $1.71 \times 10^6$. The measurements show that the slat extensions shorten the slat-cove shear layer trajectory, resulting in reduced growth of disturbances within the slat-cove shear layer. This leads to a shift of tonal peaks to higher frequencies and a reduction in the tonal amplitudes. The gap filler blocks the flow path through the gap, causing the reattachment location to shift to the main wing leading edge lower surface. Consequently, the feedback loop associated with the flow-acoustic interaction in the baseline case is eliminated, and the turbulent kinetic energy in the slat-cove shear layer is significantly reduced. However, extensive flow separation is observed on the suction side of the gap filler, which does not eliminate the noise reduction benefit due to the gap filler, but does degrade the aerodynamic performance of the high-lift configuration. Finally, the overall flow field in the presence of the cove filler is similar to that in the baseline case at the design angle of attack, but the slat-cove shear layer is eliminated, leading to a suppression of the cavity tones associated with the shear layer. This change accounts for the reduction in slat noise as measured in previous work.**

## Nomenclature

| | | |
|---|---|---|
| $c$ | = | stowed chord, [m] |
| $d$ | = | slice cut distance, [m] |
| $l$ | = | slat extension length, [m] |
| $S$ | = | shear layer trajectory length, [m] |
| $St$ | = | Strouhal number |
| $s$ | = | slat chord, [m] |
| $U_\infty$ | = | freestream velocity, [m/s] |

*Research Faculty, Department of Mechanical Engineering, AIAA Member. yz12b@my.fsu.edu
†Graduate Research Assistant, Department of Mechanical Engineering, AIAA Student Member
‡Professor and University Eminent Scholar, Department of Mechanical Engineering, AIAA Associate Fellow.
§Aerospace Technologist, NASA Langley Research Center, AIAA Fellow.
¶Research Aerospace Engineer, NASA Langley Research Center, AIAA Member.
‖Aerospace Technologist, NASA Langley Research Center, AIAA Associate Fellow.
**Aerospace Technologist, NASA Langley Research Center, AIAA Associate Fellow.
††Aerospace Technologist, NASA Langley Research Center, AIAA Associate Fellow.

$u$ = velocity in the streamwise direction, [m/s]
$v$ = velocity in the normal direction, [m/s]
$x$ = chordwise direction, [m]
$y$ = normal direction, [m]
$\alpha$ = angle of attack, [°]
$\delta_\omega$ = vorticity thickness, [m]
$\omega$ = spanwise vorticity, [1/s]

# I. Introduction

As a result of the quieter, high-bypass ratio turbofan engines on modern commercial aircraft, many of the dominant sources of noise during the landing/approach phase are associated with the unsteady flow over the airframe, rather than with the engine [1]. A deployed high-lift system contributes a significant portion of the noise radiated from an aircraft, along with the landing gear. For a multielement high-lift configuration, the leading-edge slat and the trailing-edge flap are often the dominant sources of noise from the wing [2]. Thus, much research has been conducted on the noise generation from these two components. The present work focuses on investigating potential noise treatments on leading-edge slat noise.

Figure 1 illustrates the generic flow features in the vicinity of the slat-cove region of a multielement airfoil. On the pressure side, the incoming flow separates at the slat cusp and forms a shear layer. At subscale Reynolds numbers, such as those in a number of wind tunnel experiments, the shear layer reattaches to the slat-cove surface. This leads to a flow-acoustic interaction that drives a feedback loop, analogous to that in open cavities. The resonance associated with this feedback loop results in multiple strong narrowband peaks in the mid-Strouhal number range ($1 < St_s < 5$) [3, 4], which are similar to the Rossiter modes [5] of cavity flows. The shear layer trajectory is also unsteady, and the flapping motion of the shear layer results in fluctuations of the shear layer impingement location on the slat surface. This unsteady motion induces bulk cove oscillations at low-Strouhal numbers ($St_s \approx 0.15$) [4]. Slat noise also includes a broadband component with a peak Strouhal range in the vicinity of $St_s \approx 1$ [6]. Choudhari and Khorrami [7] attribute this to unsteady vortical structures produced by the slat-cove shear layer interacting with the airfoil surfaces. This idea is corroborated by Knacke and Thiele [8], who used statistical correlation techniques to provide evidence that the principal source of the noise is due to unsteady structures interacting with the slat trailing edge. On the suction side of the slat, the flow separates at the blunt slat trailing edge and generates high-frequency noise due to vortex shedding. Indeed, time-accurate numerical simulations have provided ample evidence that slat trailing edge shedding produces a high Strouhal number spectral peak ($20 < St_s < 40$) [9, 10]. This shedding frequency scales better with a Strouhal number, based on the trailing edge thickness as the characteristic length scale, of approximately 0.2, using a local velocity in the freestream near the slat trailing edge [11].

With an understanding of the noise generation mechanisms, several noise reduction techniques have been explored. These techniques seek to reduce noise by either reducing the amplitude and/or spatial extent of flow unsteadiness, or by altering the trajectory of the slat-cove shear layer to minimize its interaction with the airfoil surfaces. The most straightforward solution to reducing or even eliminating the slat-cove shear layer is to fill the cove region, such that the region of flow separation is minimized or completely removed. In particular, a cove filler can be designed to align with the dividing streamline of the slat-cove recirculation bubble at a specific angle of attack, which helps to mitigate the noise associated with the shear layer and any associated cavity tones [12–14]. A potential drawback of the cove filler is the degradation of the noise suppression at off-design conditions. It also appears that the streamlined geometry of the slat with a cove filler allows for more orderly vortex shedding in the slat wake, resulting in a stronger noise source at the slat trailing edge shedding frequency [14]. The most recent study by Jawahar et al. [15] showed that the slat-cove filler suppressed the tonal noise, although the slat-cove shear layer was not completely eliminated as found via PIV measurements. A deformable cove filler is more suitable as it can adapt its shape for multiple flow conditions. Scholten et al. [16] designed a slat-cove filler using shape-memory alloy materials, which could potentially be adapted to allow active control of the cove filler geometry, and to permit the slat to be stowed properly for cruise.

An alternative approach to modify the slat-cove shear layer is to make geometric modifications to the slat cusp. For example, chevrons have been introduced at the cusp to enhance mixing within the shear layer, an idea that has been successfully employed to reduce jet noise [17]. Kopiev et al. [18] performed a parametric study of different heights and angles of the serrations, finding an optimal geometry that resulted in a negligible reduction in lift, but helped suppress all of the narrowband peaks within the range of $St_s = 1 - 5$. However, the noise control performance is dependent on the serration parameters, and some serrations can even increase the noise levels. Without serrations, the noise level

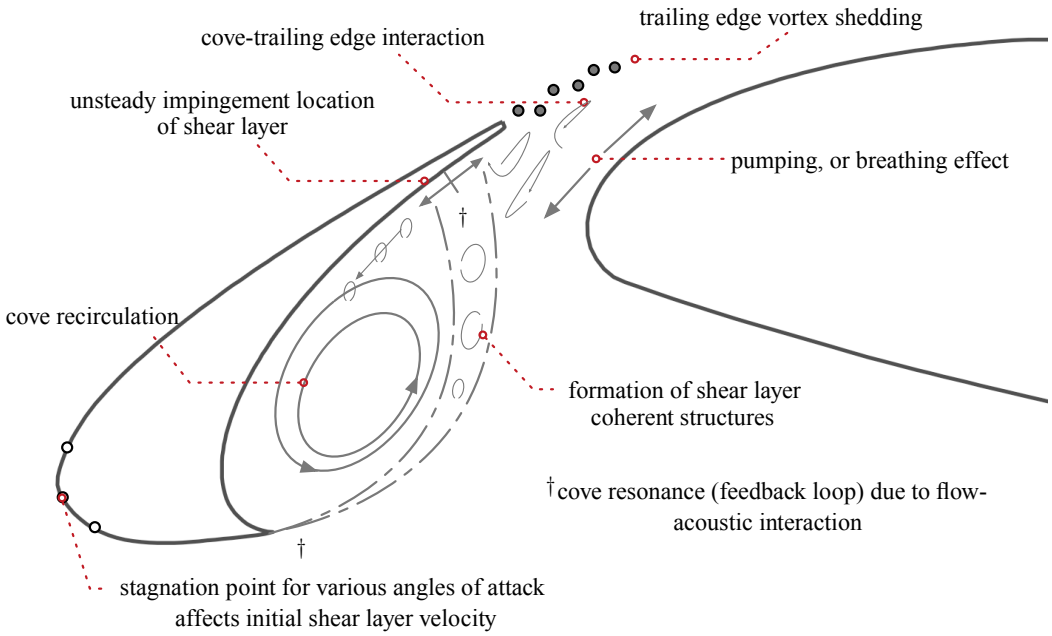


**Fig. 1 Illustration of slat noise mechanism (adapted from Ref. [7]).**

can also be reduced via an extended slat cusp [19]. The extended slat cusp delays the formation of the shear layer and presumably shortens its trajectory, which reduces the growth of disturbances due to the shear layer instability.

Pagani et al. [20] showed that the slat noise can be greatly affected by the gap overlap configuration. Increasing the gap overlap reduces the intensity of low-frequency narrowband peaks but increases the intensity of the high-frequency hump. Turner et al. [21, 22] proposed using a deformable skin element to close the gap between the slat trailing edge and main wing leading edge. In our previous studies [19, 23], a rigid gap filler successfully achieved 13 dB reduction in overall sound pressure level (OASPL) by altering the trajectory of the slat-cove shear layer. However, PIV measurements [23] were only performed on the pressure side and, therefore, the cause of the observed degradation in the aerodynamic performance was not fully understood.

In our previous studies [19, 23], the slat cusp extensions provided less noise reduction compared with the cove and gap fillers, and the observed changes in aerodynamic performance were negligible. The cove filler successfully suppressed all tonal noise, but whether or not it was able to eliminate the slat-cove shear layer could not be assessed. The gap filler was also a promising passive noise suppression device. However, the mechanism responsible for the observed aerodynamic penalty needs to be understood so that this device can be further improved for practical implementation. The goal of this study is not only to help answer these questions, but also provide additional measurements contributing to a database for the validation of future simulations. The current paper is arranged as follows. Section II provides details of the experimental arrangement. This is followed by a description of the experimental results and their discussion in Section III. Lastly, conclusions from the experimental study are presented in Section IV.

## II. Experimental setup

### A. Wind tunnel facility and 30P30N model

The current study was carried out in the Florida State Aeroacoustic Tunnel (FSAT) facility located at the Florida State University. The test section has dimensions of 2.74 m by 1.22 m by 0.91 m in the streamwise, horizontal, and spanwise directions, respectively. The two-dimensional airfoil model is mounted vertically, spanning the full height with its center of rotation located at the middle of the test section, with primary dimensions and a schematic provided in Table 1 and Figure 2, respectively. The total pressure is measured by using a pitot probe that is located approximately 0.9 m upstream of the airfoil, and the static pressure is averaged from the taps near the end of the contraction, in order to avoid effects of blockage due to the model. The pitot probe measurement is then corrected on the basis of the area ratio.

All the measurements are taken at $\alpha = 5.5°$ and a stowed-chord-based Reynolds number of $Re_c = 1.71 \times 10^6$, with a corresponding Mach number of 0.17. The coordinate system is aligned such that the $x$-axis represents the chordwise direction and the $y$-axis is normal to the airfoil stowed chord line, with its origin at the leading edge of the stowed airfoil.

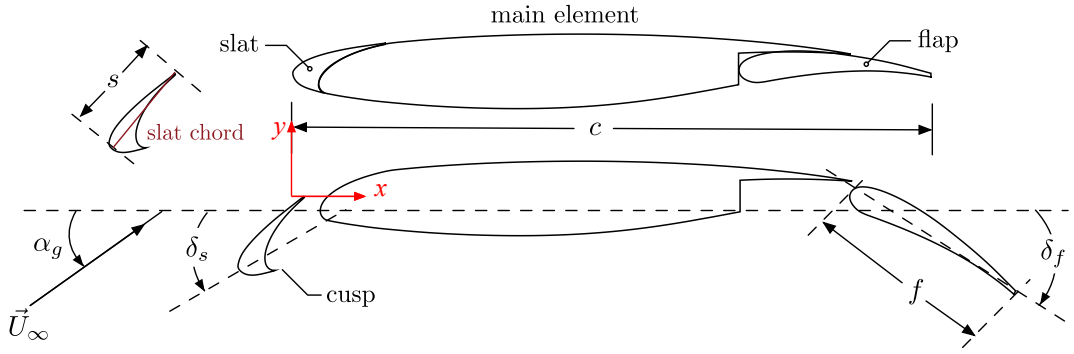


**Fig. 2 Schematic of the 30P30N multielement airfoil (adapted from Ref. [11]).**

**Table 1 Primary dimensions of 30P30N airfoil.**

| | | |
|---|---|---|
| Stowed chord | $c$ | 0.457 m |
| Span length | $b$ | 0.914 m |
| Slat chord | $s$ | $0.15c$ |
| Flap chord | $f$ | $0.3c$ |
| Slat deflection angle | $\delta_s$ | 30° |
| Flap deflection angle | $\delta_f$ | 30° |

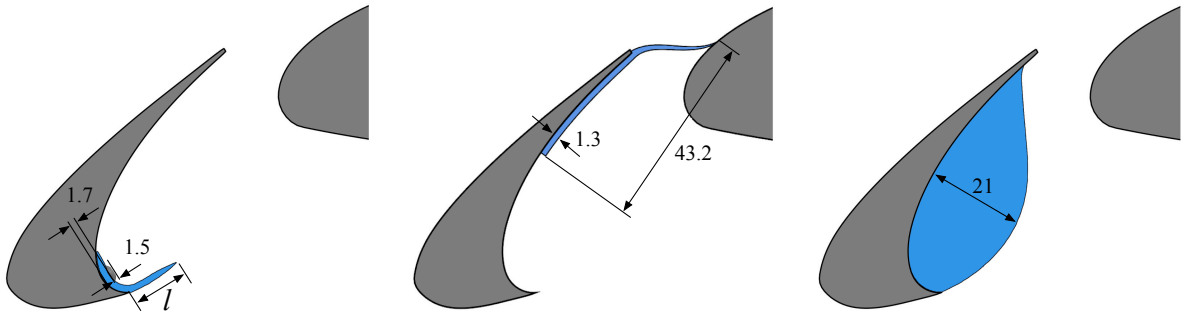


**(a) Slat extension** **(b) Gap filler** **(c) Cove filler**

**Fig. 3 Schematic of passive noise control devices considered in the present work (units in mm).**

The baseline case is illustrated in Figure 2, where the slat and flap are deployed. To alter the flow field around the slat and investigate acoustic impacts, three treatments were designed and tested: slat cusp extensions, a gap filler, and a cove filler. Schematics of these devices are shown in Figure 3. The details of these treatments and their assessments in terms of flow control performance are presented in our previous studies [19, 23]. Three slat cusp extensions are tested, namely, $Ext_s$, $Ext_m$, and $Ext_l$, that denote the short, medium, and long extensions. A schematic of the slat extensions is shown in Figure 3a. The extension lengths measured from the slat cusp are $l = 8.4$ mm, 12.5 mm, and 16.3 mm. A gap filler (Figure 3b) is a device that is designed to close the gap between the slat and the main element to prevent flow. The addition of a gap filler produces a major change in the trajectory of the shear layer. Our previous study [23] outlined the time-resolved PIV measurements in the vicinity of the slat-cove region for both the baseline and the gap filler cases, and the current study describes additional (non time-resolved) measurements on the suction side of the gap filler. Figure 3c shows the cove filler, whose streamlined profile was designed on the basis of a computed, time averaged flow field within

the slat-cove region at a free-air angle of attack equal to 5.5°. It should be noted that the cove filler does not extend all the way to the slat trailing edge, but terminates in the vicinity of the mean reattachment location in the baseline case.

### B. PIV setup

A schematic of the PIV setup is provided in Figure 4a. Due to the complicated geometry of the multielement airfoil, shadow regions would appear if the model was only illuminated on one side. Therefore, the laser beam from an Evergreen 400 mJ Nd:YAG laser is split by a cubic beamsplitter to form two laser beams. Each laser beam passes through different combinations of optics and forms laser sheets to illuminate the slat region at the mid-span plane of the model from the pressure and suction side, respectively. By using this configuration, the shadow region is significantly reduced, leaving two small blank areas behind the slat cusp and near the leading edge of the main wing, respectively. Two Imager sCMOS cameras (2560 × 2160 pixels) are secured underneath the acrylic side wall with the optical axes orthogonal to the laser sheets (Figure 4b). To capture the small field of view, the two cameras are equipped with different combinations of lenses and are located at different distances from the laser sheets. This allows for a small overlap region required to stitch the vector fields together. The camera viewing the pressure side of the slat region is equipped with a SIGMA 105 mm f/2.8 macro lens with a 1.4× teleconverter, while the other one is equipped with a TAMRON 180 mm f/3.5 macro lens with a 27.5 mm spacer. Two 532 nm bandpass filters are used to remove ambient light. Fluorescent orange tape (3M) is applied on the model surface to reduce the laser reflections. Calibration is performed prior to the data acquisition with a LaVision type-22 calibration plate. Olive oil is used in a TSI 9307-6 seeder to generate the tracing particles, which are injected into the flow downstream of the inlet screen. The double-frame image pairs are acquired at a sampling rate of 10 Hz with a nominal number of 550 vector fields obtained for each case using LaVision DaVis 8.4.0 software.

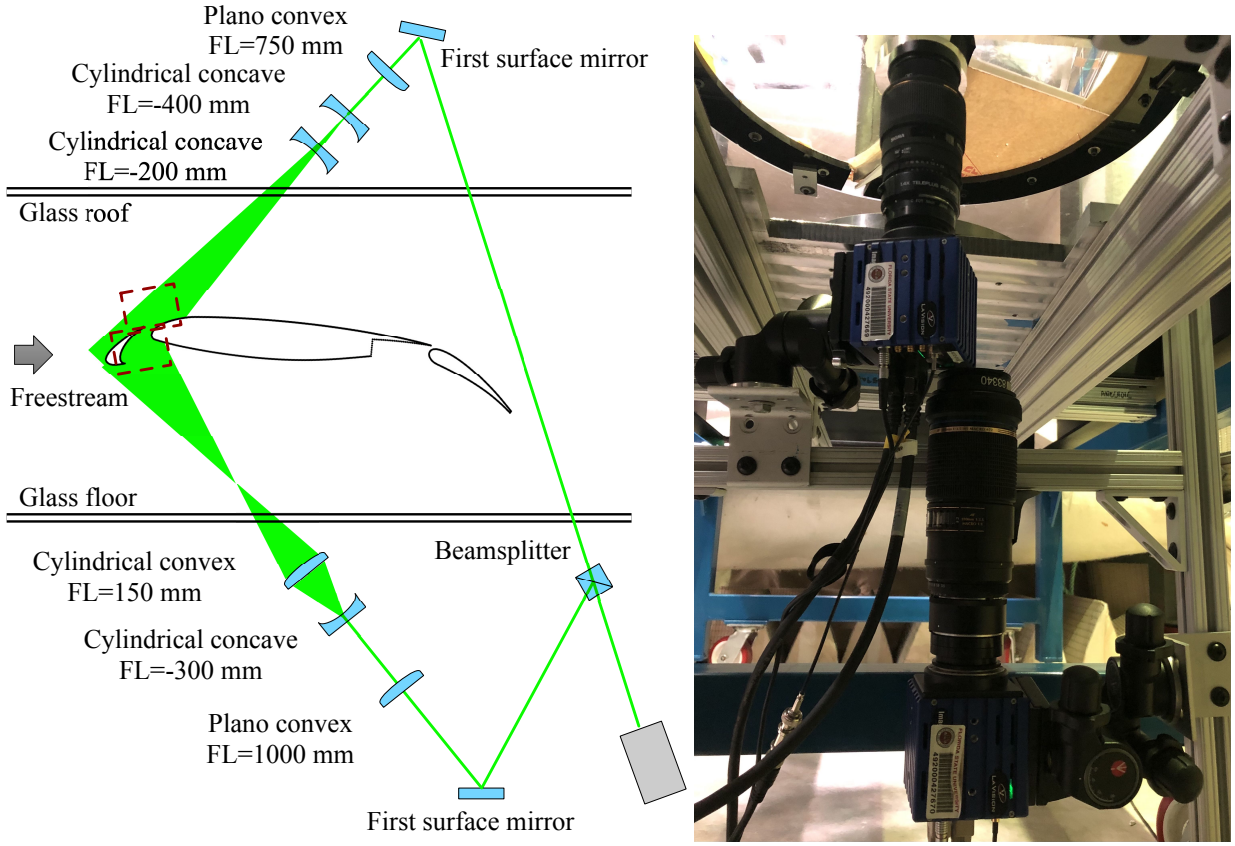


**(a) Schematic of PIV (not to scale)** **(b) PIV cameras**

**Fig. 4 PIV experiment setup.**

The data are processed using the same software as that used for the data acquisition. For each data set, the background

image is first subtracted from the instantaneous measurements to enhance the signal-to-noise ratio. Geometric and algorithmic masks are applied on the domain to cover the model geometry and low seeding density regions. Then, a multipass cross-correlation scheme using window sizes ranging from $256 \times 256$ pixels to $32 \times 32$ pixels is used to obtain the particle displacements between image pairs. Universal outlier detection [24] is applied to remove the spurious vectors, and then the resulting two vector fields from each camera are merged. The stitched vector field is finally post-processed using multivariate outlier detection [25] in MATLAB. The resulting vector resolution is approximately 5.4 vectors/mm. The PIV results are presented in a coordinate system that has been rotated by the 5.5-degree angle of attack, such that the 30P30N model is at 0°. Therefore, the $x$-direction is aligned with the stowed chord at a zero degree angle of attack and it does not represent the direction of the incoming flow.

## III. Results and discussion

### A. Slat extensions

The time-averaged velocity components of the baseline case and the slat extension cases are given in Figures 5 and 6. The baseline results in Figures 5a and 6a basically reproduce the results of Pascioni and Cattafesta [26]. The flow features in the slat-cove vicinity are generally similar in both the baseline and slat extension cases. The flow separates at the slat cusp and reattaches to the cove surface, and a large recirculation bubble is enclosed by the mean shear layer. At the leading edge of the main element, the freestream flow below the slat-cove region impinges on the pressure side of the main wing, and the flow accelerates to pass through the gap between the slat and the main wing. The use of slat extensions has a minimal effect on the stagnation location on the main wing in comparison to the baseline case. Not only are the spatial distributions of both velocity components very similar between the baseline and the treated cases, but the time-averaged spanwise vorticity (Figure 7) and the turbulent kinetic energy (TKE) (Figure 8) are also similar in terms of their spatial variation and their amplitude levels. High vorticity magnitudes are mainly encountered in the slat-cove shear layer and the shear layer behind the slat trailing edge. The vorticity is greatest near the slat cusp and then decays as the shear layer thickens along its trajectory in a time-averaged sense. The vorticity in the slat trailing edge shear layer exhibits both positive and negative values as shown by the red and blue contours. The TKE is highest near the separation points and then decreases along the length of the separation zone. The TKE is also high near the shear layer reattachment points. By comparing the baseline case with the slat extension cases, it is observed that the high TKE near the reattachment point in the baseline case exhibits a slightly higher level and extent than the slat extension cases. For instance, the TKE peak level in the reattachment vicinity is reduced approximately 4% in the $Ext_l$ case compared with the baseline case. Note that the longest extension $Ext_l$ achieved the highest reduction of approximately 5 dB in OASPL among the tested slat extensions in our previous study [19].

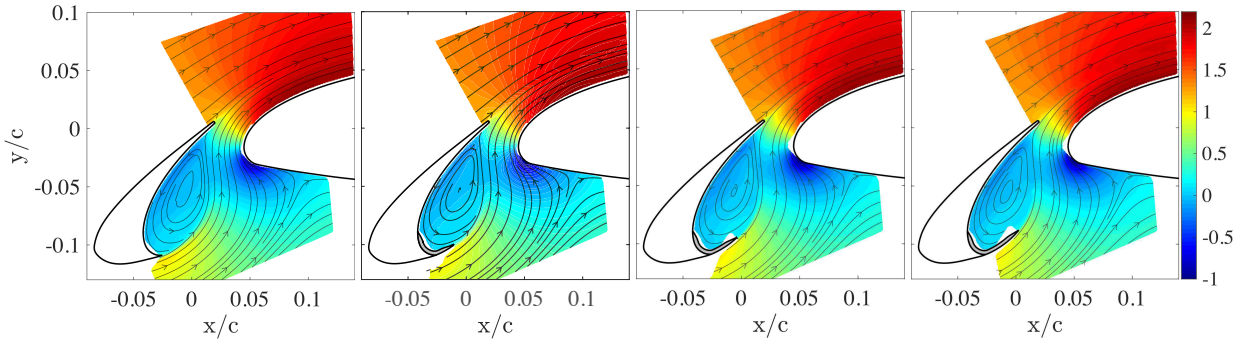


**(a) Baseline** **(b)** $Ext_s$ **(c)** $Ext_m$ **(d)** $Ext_l$

**Fig. 5 Time-averaged $\overline{u}/U_\infty$ velocity component of baseline case versus slat extension cases with streamlines at $\alpha = 5.5°$.**

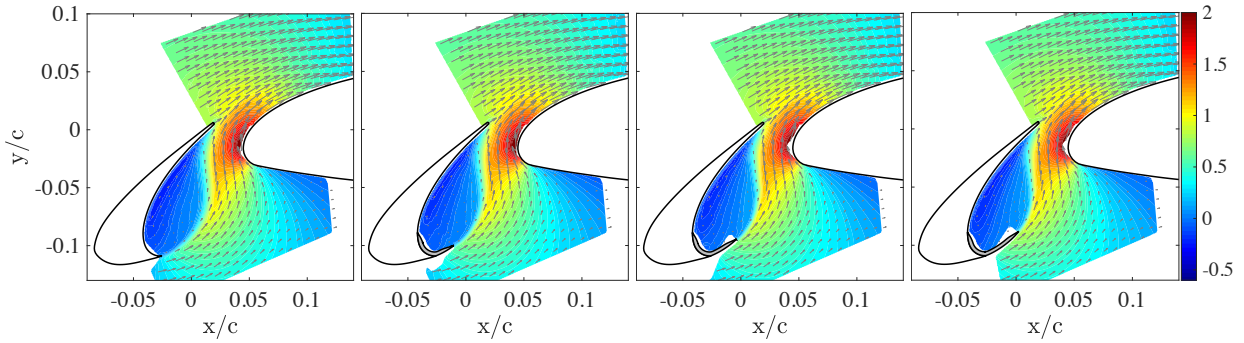


**(a) Baseline** **(b)** $Ext_s$ **(c)** $Ext_m$ **(d)** $Ext_l$

**Fig. 6 Time-averaged $\overline{v}/U_\infty$ velocity component of baseline case versus slat extension cases with vectors overlaid at $\alpha = 5.5°$.**

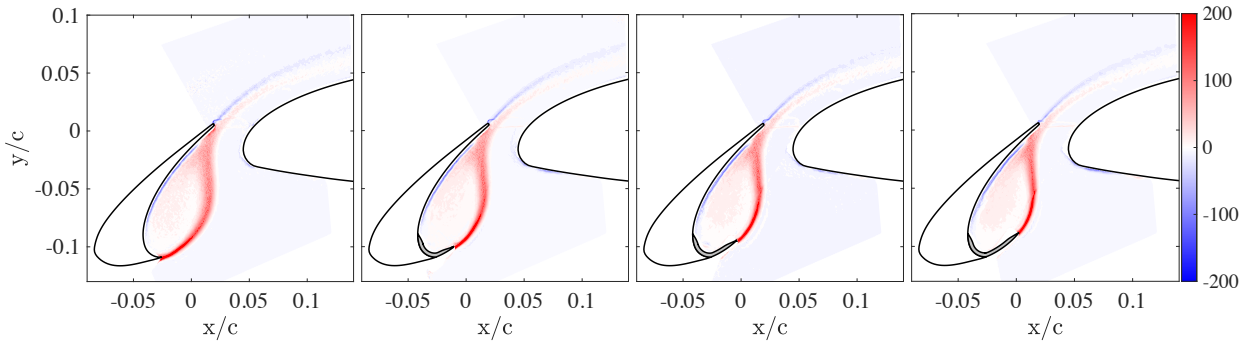


**(a) Baseline** **(b)** $Ext_s$ **(c)** $Ext_m$ **(d)** $Ext_l$

**Fig. 7 Time-averaged spanwise vorticity $\overline{\omega}c/U_\infty$ of baseline case versus slat extension cases at $\alpha = 5.5°$.**

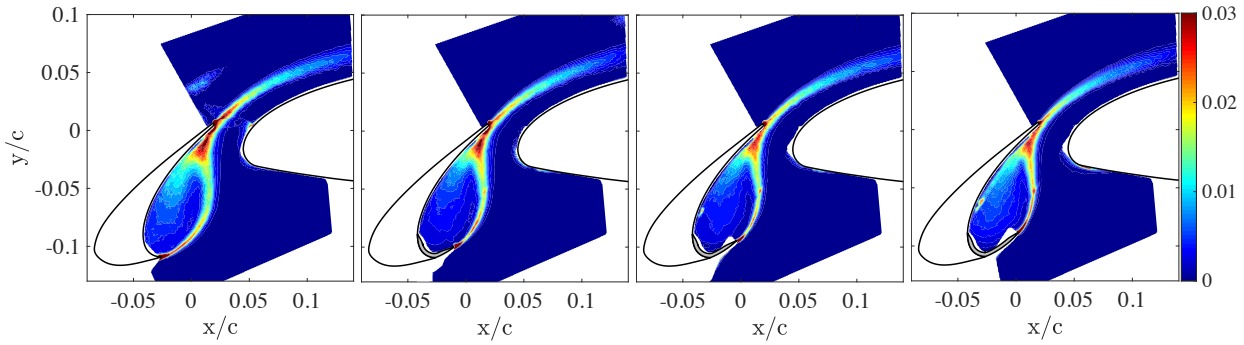


**(a) Baseline** **(b)** $Ext_s$ **(c)** $Ext_m$ **(d)** $Ext_l$

**Fig. 8 TKE $\overline{(u'^2 + v'^2)}/(2U_\infty^2)$ of baseline case versus slat extension cases at $\alpha = 5.5°$.**

In order to study the characteristics of the mean shear layer, the mean shear layer trajectories are approximated by tracking the highest level of TKE along the shear layer. The path and slices normal to the local slope are highlighted as dashed lines and solid lines, respectively, in Figure 9. The local origin of each shear layer path is defined at the slat cusp or extension tip. The slices are at $S/S_\mathrm{b} = 0.1, 0.2, 0.3, \ldots, 0.8$, where $S_\mathrm{b}$ is the total arclength of the baseline shear layer. The profiles along the slices are plotted as a function of the normalized distance $d/c$ within the range of [-0.02, 0.02], with the positive direction pointing outward from the recirculation bubble (as illustrated in Figure 9). The length

of the shear layer for each case is summarized in Table 2, and the change in the shear layer trajectory and the center of the recirculation bubble is depicted in Figure 10. With the slat extensions, the reattachment location on the cove surface shifts slightly toward the slat trailing edge. The alteration of the shear layer trajectory is minor and is similar between the different slat extensions, as the design of the extensions was essentially following the natural shear layer trajectory of the baseline case from simulation [7]. The center of the recirculation bubbles shows a trend of moving toward the slat leading edge with the increase of the slat extension length.

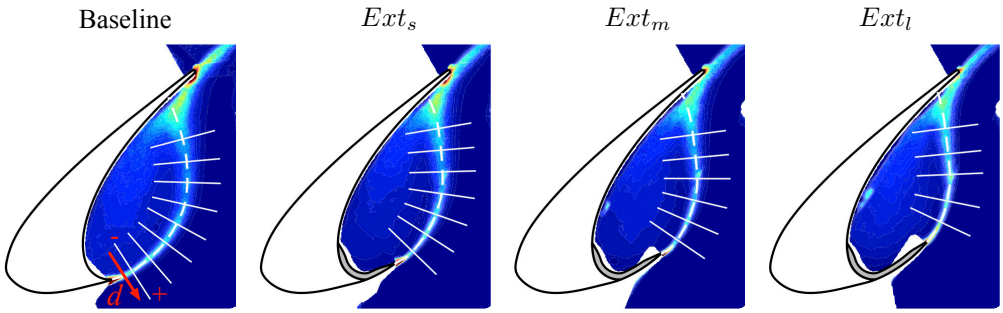


**Fig. 9 Slices of slat-cove shear layer for baseline and slat extension cases.**

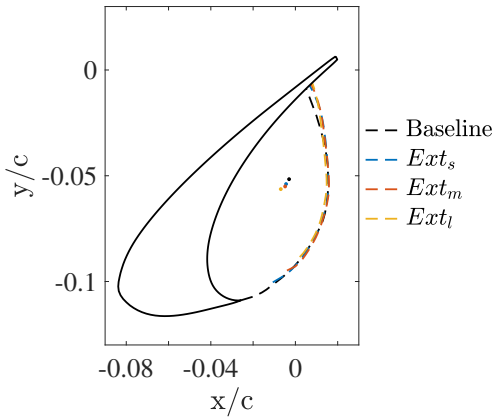


**Fig. 10 Shear layer trajectories and center of recirculation bubbles for baseline and slat extension cases.**

**Table 2 Approximated slat-cove shear layer length for baseline and slat extension cases.**

| Case | Baseline | $Ext_s$ | $Ext_m$ | $Ext_l$ |
|---|---|---|---|---|
| $S_{\max}/c$ | 0.120 | 0.104 | 0.096 | 0.086 |

Data along the slices are interpolated over two-dimensional grids based on a cubic convolution. As reattachment stops the shear layer from natural growth, the slices near the reattachment region are ignored. The TKE and spanwise vorticity are extracted from each slice and are compared in Figure 11. As the shear layer trajectory is approximated based on local maximal TKE in each case, the peaks are centered at $d/c = 0$. The circulation bubble ($d/c < 0$) exhibits a higher TKE level than the freestream ($d/c > 0$) as expected. The vorticity profile is quite symmetric near the shear layer origin (slat cusp), and the profile is skewed towards positive $d/c$ at $S/S_b = 0.7$ and 0.8 locations. The profiles for the baseline and three extensions cases generally overlap closer to the origin of the shear layer, and the discrepancy increases as the shear layer approaches reattachment near the slat trailing edge. For instance, the main discrepancies in Figure 11a are $Ext_s$ at $S/S_b = 0.7$, $Ext_m$ at $S/S_b = 0.6$, and $Ext_l$ at $S/S_b = 0.5$. It should be noted that some discrepancies exist for $Ext_l$ at $S/S_b = 0.3$, which are due to the spurious results along the edge of overlapped laser sheets. The velocity components are projected locally tangential to the shear layer curve along the slice to characterize the

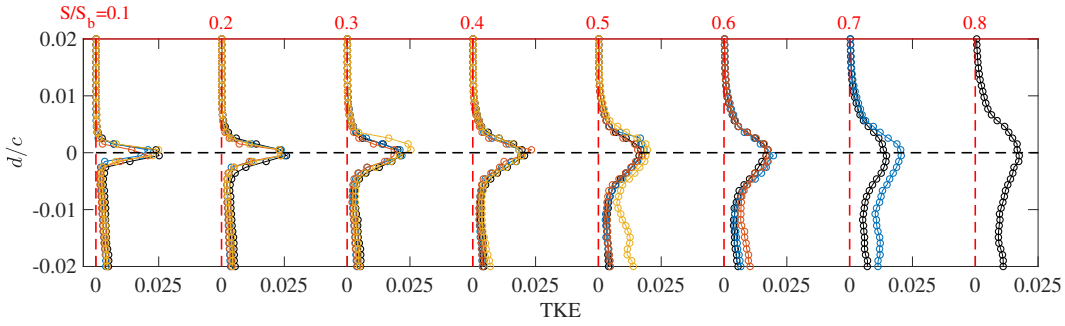


**(a) Slices of TKE**

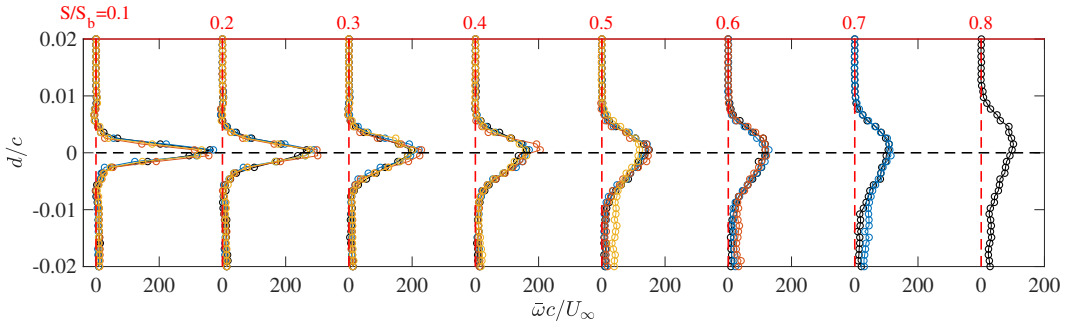


**(b) Slices of vorticity**

**Fig. 11 Slices of TKE and vorticity in the slat-cove shear layer. ∘: baseline; ∘: $Ext_s$; ∘: $Ext_m$; and ∘: $Ext_l$.**

growth of the shear layer. Then the local vorticity thickness is calculated as $\delta_\omega = U_{\text{edge}}/(\partial u/\partial d)_{\text{max}}$, where $U_{\text{edge}}$ is the tangential velocity at $d/c = 0.02$. The vorticity thicknesses for all cases are compared in Figure 12. Beyond an initial region of up to $S/S_b = 0.3 - 0.4$, the increase in vorticity thickness is nearly linear. The shear layer thickness for the slat extension cases is slightly thinner in comparison with that in the baseline case. However, the growth curves nearly overlap across all cases, indicating that the slat extensions have a minimal effect on the growth of the mean shear layer.

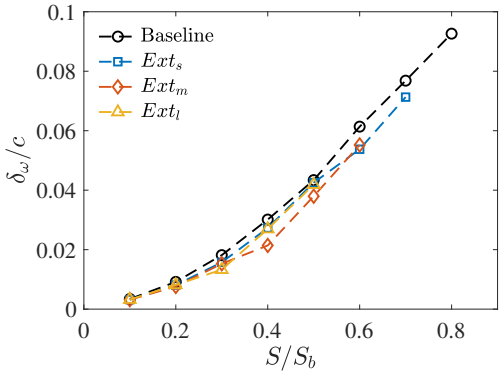


**Fig. 12 Nondimensional vorticity thickness for baseline and slat extension cases.**

The main effect of the slat extensions is the shortened shear layer trajectory path. As a result, the local unsteady surface pressure and far-field acoustic fluctuations are both suppressed, and the tones are shifted to higher frequencies, as noted in our previous study [19]. An example comparison between the integrated Sound Pressure Level (SPL) for the baseline and slat extensions is shown in Figure 13. The tonal peaks shift to higher frequencies with the increase of the extension length in Figure 13a. With a rescaled Strouhal number based on the shear layer length given in Table 2, the tonal frequencies indicate a good collapse across the four cases as shown in Figure 13b, indicating that the shear layer length is the proper length scale to characterize the tonal frequencies.

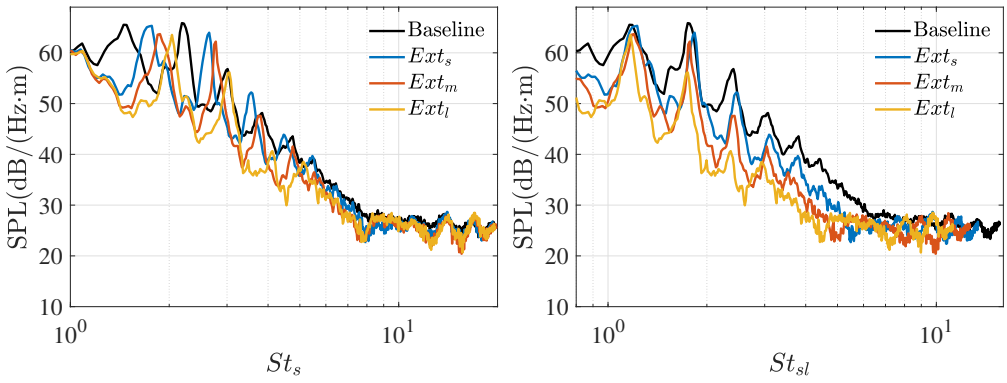


**(a) Scaled using slat length ($s$) [19]** **(b) Scaled using slat-cove shear layer length ($S_{\max}$)**

**Fig. 13 Reproduced integrated SPL for baseline and slat extension cases with Strohaul numbers based on different length scales at $\alpha = 5.5°$ and $Re_c = 1.71 \times 10^6$ from previous study.**

Although the slat extensions are designed to alter the slat-cove shear layer, they can also affect the pumping/breathing effects of the flow through the gap, leading to changes in the vortex shedding from the slat trailing edge shear layer. Therefore, the flow fields are compared at the slices of the shear layer from the slat trailing edge, which are labeled as $w_1, w_2, \cdots, w_{10}$ in Figure 14. The slices are orthogonal to a line emanating normal to the base of the trailing edge at its midpoint. The streamwise locations of these cuts are chosen to be in equal logarithmic increments. The normalized slices ($d/c$) are from -0.02 to 0.02 with the positive direction pointing toward the airfoil, and the slice cut centers are given in Table 3.

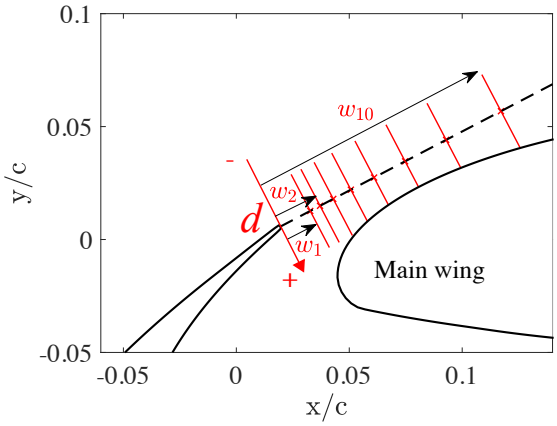


**Fig. 14 Slices of slat trailing edge shear layer for baseline and slat extension cases.**

**Table 3 Slices of slat trailing edge shear layer for baseline and slat extension cases. Distance is normalized by $c$ ($\times 10^{-3}$).**

| $w_1$ | $w_2$ | $w_3$ | $w_4$ | $w_5$ | $w_6$ | $w_7$ | $w_8$ | $w_9$ | $w_{10}$ |
|---|---|---|---|---|---|---|---|---|---|
| 6.86 | 9.09 | 7.54 | 16.13 | 21.43 | 28.52 | 37.89 | 50.41 | 67.00 | 89.12 |

The vorticity and TKE profiles for the baseline and slat extension cases are compared in Figure 15. The TKE peak level decays along the downstream direction. It is clear that the baseline case exhibits a higher TKE peak level than the slat extension cases. Among the slat extension cases, the longest extension results in the largest reduction in the TKE peak level, which is presumably due to the reduced flapping motion of the slat-cove shear layer. The vorticity profile shows both positive and negative peaks, indicating that vortices with opposing rotation are shed from the two sides of the slat trailing edge. It should be noted that the negative direction of $d/c$ points to the upper portion (freestream

side) and positive values of $d/c$ point to the lower portion (airfoil side) of the vortex shedding, respectively. The vortex shedding on the freestream side is stronger in amplitude. The effects of slat extensions on the vorticity profiles are not statistically significant, because all profiles match to within experimental uncertainty at each slice cut location. The overall effects of the slat extensions on the slat trailing edge vortex shedding are rather weak, such that the local surface pressure fluctuations near the slat trailing edge are barely affected, as demonstrated in our previous study [19].

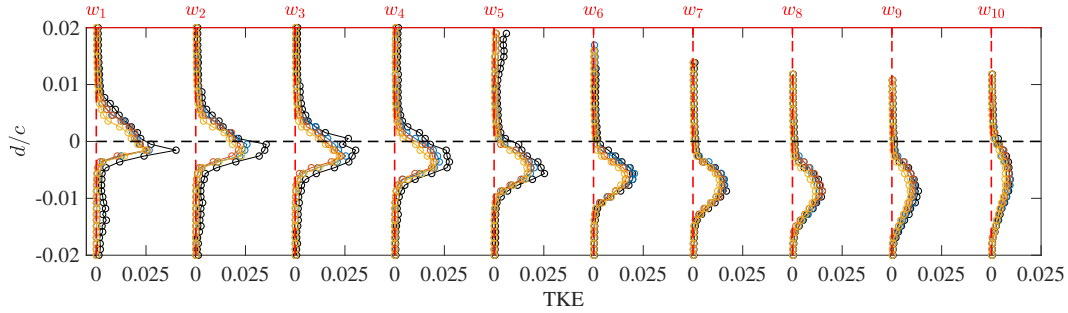


**(a) Slices of TKE**

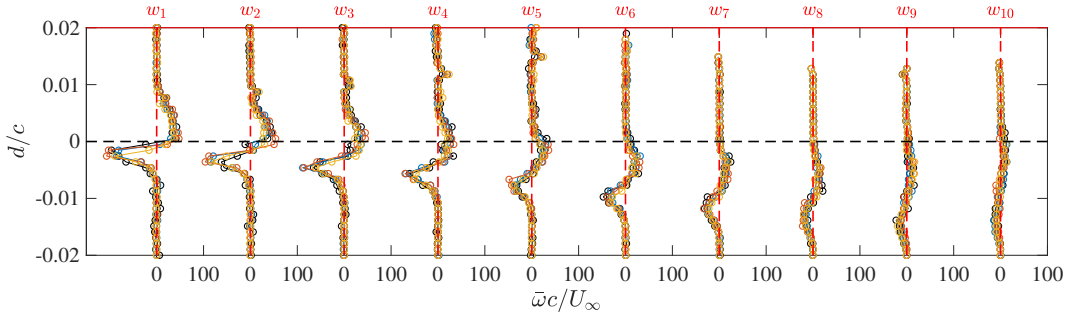


**(b) Slices of vorticity**

**Fig. 15 Slices of TKE and vorticity in the slat wake. ○: baseline; ○: $Ext_s$; ○: $Ext_m$; and ○: $Ext_l$. Note that $d/c = 0$ was chosen for a line originating at the slat trailing edge as in Figure 14 but not the shear layer trajectory.**

### B. Gap filler and cove filler

This section will address both the gap filler and cove filler for direct comparisons with the baseline case. In Figures 16b and 17b, with the gap filler installed, the slat-cusp shear layer no longer reattaches to the cove surface. Instead, the slat-cusp shear layer trajectory is relatively straight. Although the current field of view does not fully capture the slat-cusp shear layer reattachment, it has been shown to reattach to the main wing lower surface in our previous study [23]. This results in a larger recirculation region enclosed by the shear layer. A secondary smaller recirculation bubble is present below the gap filler at the corner between the gap filler and the main wing. These time-averaged results of the cove-side flow field reproduce the time-averaged results of our previous time-resolved PIV measurements [23]. In the current study, we extended the measurement domain to the upper (suction) side of the gap filler, where the flow separates at the joint of the slat trailing edge and the gap filler. It should be noted that the present gap filler profile is not optimized for reducing the flow separation. It is clear that the higher speed external flow above the slat in the gap filler case results in lower surface pressure on the slat suction side, while the flow separation leads to increased pressure on the leading edge of the main element on the suction side, as shown in Figure 18a. The effects on the lift coefficient are the increase of lift on the slat portion and penalty in the total lift, as shown in Figure 18 below from our previous study [23]. However, the flow separation issue could be resolved or improved if the gap filler profile is more streamlined, and thus the aerodynamic penalty with the implementation of the gap filler can be reduced. A similar concept was tested on a 1/16th scale NASA High Lift Common Research Model recently, and negligible loss or even some small improvement in lift was observed with different gap filler configurations installed [27].

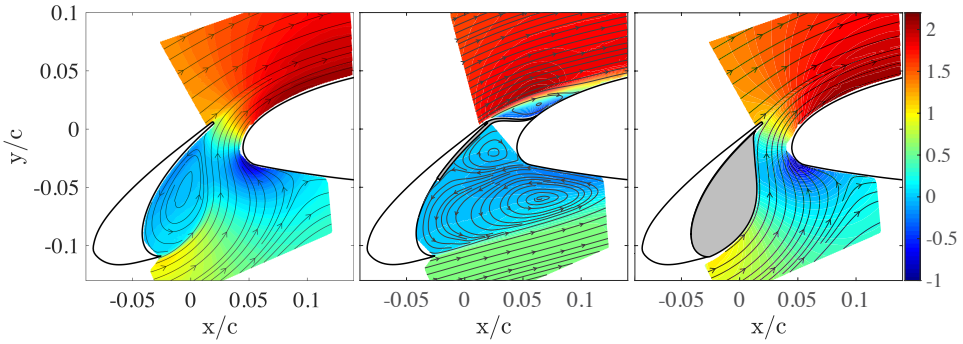


**(a) Baseline** **(b) Gap filler** **(c) Cove filler**

**Fig. 16 Time-averaged $\overline{u}/U_\infty$ velocity component of baseline case versus gap filler and cove filler cases with streamlines at $\alpha = 5.5°$.**

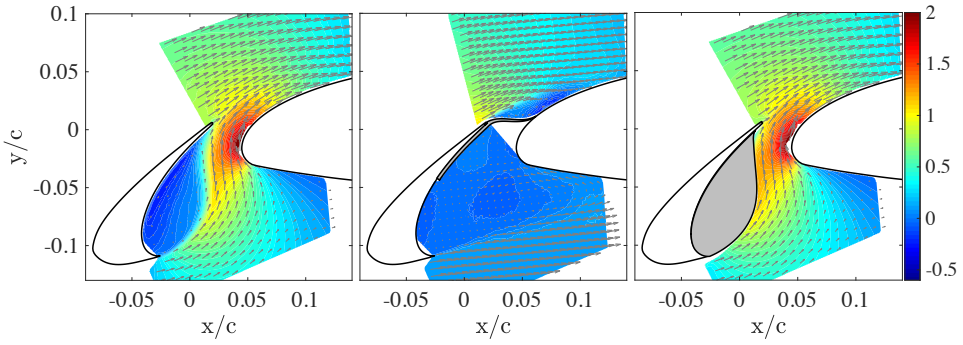


**(a) Baseline** **(b) Gap filler** **(c) Cove filler**

**Fig. 17 Time-averaged $\overline{v}/U_\infty$ velocity component of baseline case versus gap filler and cove filler cases with vectors overlaid at $\alpha = 5.5°$.**

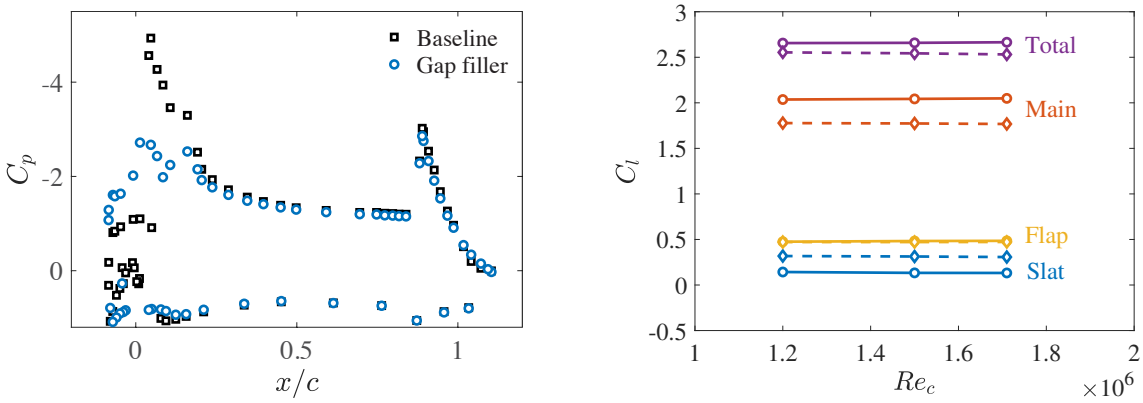


**(a) $C_p$ distribution at $Re_c = 1.71 \times 10^6$**

**(b) Lift coefficient $C_l$ at different $Re_c$. Rigid lines: baseline; dashed lines: gap filler.**

**Fig. 18 Aerodynamic penalty with gap filler installed (reproduced from Ref. [23]).**

Turning attention to the slat cove filler case shown in Figures 16c and 17c, begin by recalling that the slat-cove filler was designed based on the streamline of the baseline case at the angle of attack of 5.5°. The slat-cove shear layer is totally eliminated, and the flow field is quite similar to the baseline case except that the cove region is covered by

the filler. The flow remains attached to the cove filler surface, and the flow over the cove filler surface has a slightly higher speed than the flow surrounding the shear layer in the baseline case, as seen from the comparison of the velocity magnitudes in Figure 19. Then, the flow decelerates when approaching the slat trailing edge and eventually separates at the slat trailing edge tip (Figure 19b).

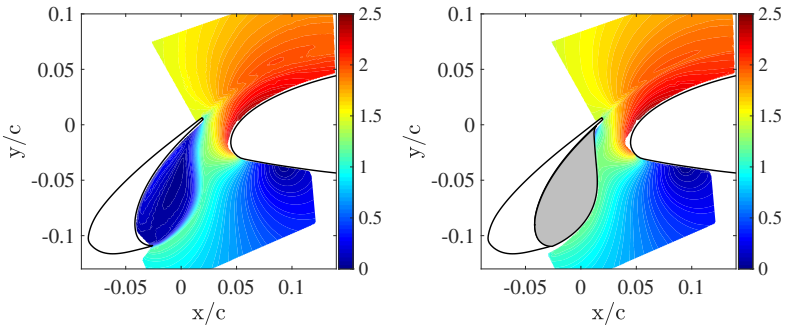


**(a) Baseline** **(b) Cove filler**

**Fig. 19 Velocity magnitude $\sqrt{\overline{u}^2 + \overline{v}^2}/U_\infty$ of baseline case versus cove filler case at $\alpha = 5.5°$.**

The positive vorticity in the gap filler case (Figure 20b) indicates a straight slat-cove shear layer directed at the pressure side of the main wing, as compared with the curved one showing reattachment near the slat trailing edge in the baseline case. Note that the vorticity contour plot is using the same color scale across all subplots, therefore, the high vorticity region near the slat cusp clearly has a narrower extent in the gap filler case. At the upper side of the gap filler, a large wake region is observed, extending over a wide extent of the forward portion of the main wing. With the cove filler installed (Figure 20c), the flow does not separate at the slat cusp and remains attached all the way until it approaches the slat trailing edge, where a high level of positive vorticity is observed (Figure 20c). The shear layer formed at the slat trailing edge follows a similar path as in the baseline; however, the extent of the high vorticity region is thinner.

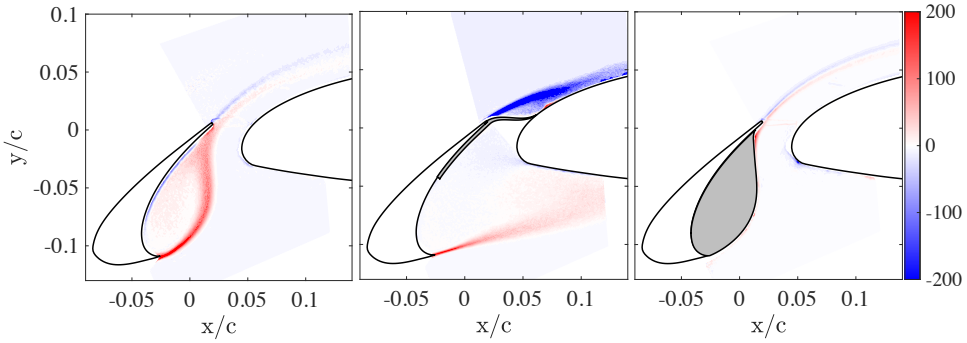


**(a) Baseline** **(b) Gap filler** **(c) Cove filler**

**Fig. 20 Time-averaged spanwise vorticity of baseline case versus gap filler and cove filler cases at $\alpha = 5.5°$.**

Figure 21b shows that the TKE levels in the slat-cove shear layer are significantly suppressed in the gap filler case (also note the difference in the color bar scale). This alteration of the slat-cove shear layer results in the break up of the flow-acoustic feedback phenomenon that is present in the baseline case, which leads to the suppression of slat noise, as observed in our previous study [19]. Without acoustic feedback, the multiple narrowband peaks disappear in the far-field acoustic spectra, as shown in Figure 22a reproduced from our previous study [23]. Although the wake region above the gap filler exhibits a significantly higher level of TKE, indicating larger fluctuations, these fluctuations do not propagate to the far field under the wing due to the absolute blockage by the gap filler. As a result, the far-field acoustic SPL is significantly reduced, with an approximately reduction of 13 dB in OASPL [23]. In the cove filler case (Figure 21c), not only is the slat-cove shear layer eliminated, but the high TKE extent in the trailing edge shear layer is also significantly reduced. These observations are similar to the simulation results of a similar cove filler configuration [28]. The elimination of the slat-cove shear layer leads to a quieter environment in the far-field SPL with a 14 dB reduction in

OASPL, as shown in Figure 22b reproduced from our previous studies [19].

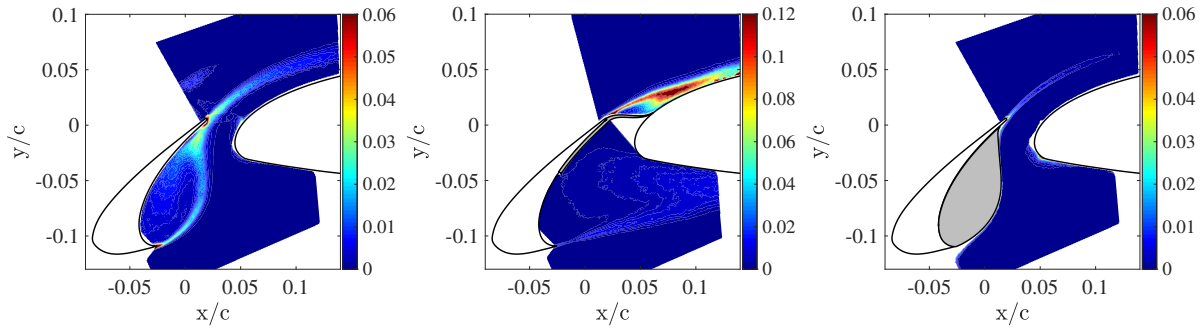


**(a) Baseline** **(b) Gap filler** **(c) Cove filler**

**Fig. 21 TKE of baseline case versus gap filler and cove filler cases at $\alpha = 5.5°$.**

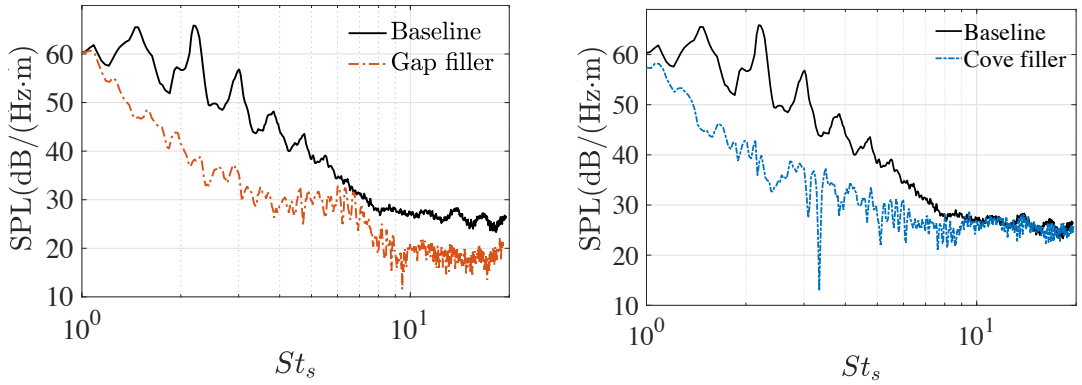


**(a) Baseline vs. Gap filler [23]** **(b) Baseline vs. Cove filler [19]**

**Fig. 22 Reproduced integrated SPL for the baseline vs. gap filler and cove filler, respectively, at $\alpha = 5.5°$ and $Re_c = 1.71 \times 10^6$ from previous studies.**

Similar to the analysis of the profiles in the previous section, the flow properties are extracted from the slat-cove shear layer at the locations depicted in Figure 23 and from the slat trailing edge shear layer as in Table 3, respectively. Although a free shear layer is not formed (rather a boundary layer along the cove filler surface), the cove filler profile generally matches the baseline shear layer trajectory except near the reattachment point (see the dashed line in the cove filler case of Figure 23). Therefore, the slice locations from the baseline case are used in the cove filler case for a fair comparison. The comparison of the TKE and vorticity profiles for the three cases are shown in Figure 24. The cove filler case shows negligible TKE and weak vorticity compared with the baseline and gap filler case, as the flow separation near the slat cusp is eliminated by filling the cove. Therefore, the following discussions will be focused on the comparisons between the gap filler and baseline cases.

The comparison of the TKE profiles indicates that the energy level of the separated flow in the gap filler case is much lower than the baseline case at all slice locations. The peak level of TKE in the gap filler case first grows along the shear layer trajectory and then decays, which is different from the monotonic decay in the baseline case. This change in TKE evolution may be due to the near absence of any recirculating vortices within the modified separation region, and the lack of an associated feedback to the cusp region. The fluctuations are significantly stronger near the separation point in the baseline case, indicating the enhanced disturbances in the upstream slat-cusp shear layer due to acoustic feedback via a receptivity process analogous to cavity flows [29, 30]. Without acoustic feedback, the TKE peak levels within the slat-cusp shear layer in the gap filler case are less than half of the baseline case at $S/S_b = 0.1$ and 0.2 locations and are approximately half of the baseline case at the other locations. In addition to the suppression of the tones, the broadband reduction is also due to the fact that separated flow with high TKE phenomena does not impinge onto any surface, leading to a significantly quieter far field as was also noted in the previous study [19, 23]. The vorticity along

the shear layer decays faster in the gap filler case (Figure 24b). By comparing the vorticity thickness in Figure 25, the two cases seem to have comparable vorticity thicknesses near the slat cusp. However, the vorticity thickness becomes significantly greater in the gap filler case as the flow develops. The shear layer diffuses over a shorter distance in the gap filler case than the baseline case, leading to a less energetic shear flow.

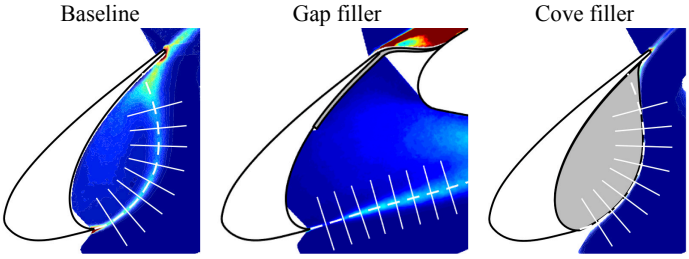


**Fig. 23 Slices of slat-cove shear layer for baseline, gap filler, and cove filler cases.**

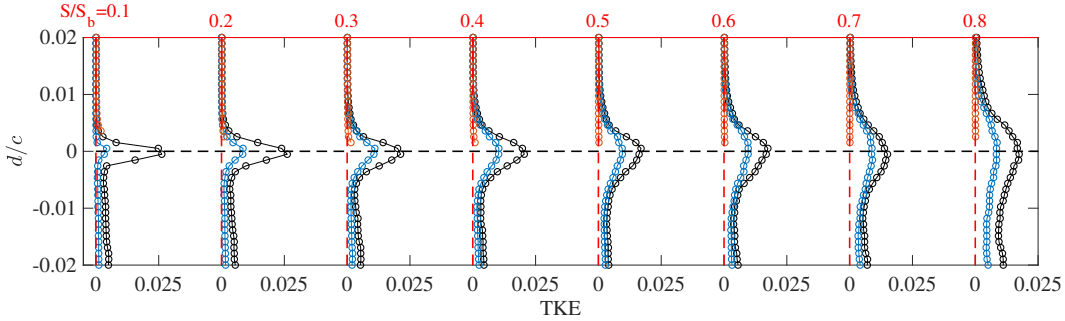


**(a) Slices of TKE**

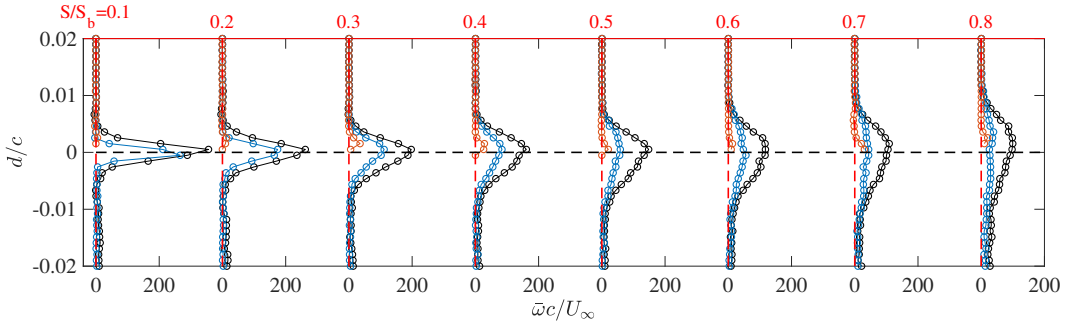


**(b) Slices of vorticity**

**Fig. 24 Slices of TKE and vorticity in the slat-cove shear layer. ○: baseline; ○: Gap filler; and ○: Cove filler.**

Now we turn our attention to the slat trailing edge shear layer. Because the characteristics of the trailing edge shear layer in the gap filler case are completely different from all other cases, and the amplitudes of peak vorticity and TKE are at least one order of magnitude larger, the profiles of the gap filler case are not compared with the baseline and cove filler cases. The slices are obtained at the same locations as in Table 3 from Section III A. In Figure 26a, the peak of TKE profiles in the cove filler case indicates a slightly deflected shear layer away from the main element, as the peaks are located below those in the baseline case. In addition, the peak levels are significantly reduced to approximately half that of peak level in the baseline case. In the vorticity profiles (Figure 26b), the negative peaks are approximately at the same level for both the baseline and cove filler cases, which means that the vortex shedding from the upper slat surface is only weakly affected. However, the peaks of positive vorticity move downward towards negative $d/c$, and with a more confined peak profile. The positive vorticity peak levels become large in the cove filler case, which implies a more orderly vortex shedding from the lower slat-cove filler surface. This is due to a lack of slat-cove shear layer interaction as found in the baseline case, in which the shear layer impingement disrupts the flow just upstream of the trailing edge.

Corroborating this observation, an increase in the tonal peak amplitude (of nearby surface fluctuating pressure or far field acoustics) associated with trailing edge vortex shedding at $St_s \in (20, 30)$ was observed in similar previous studies [14, 19, 28], also indicating a more orderly vortex shedding with the cove filler installed.

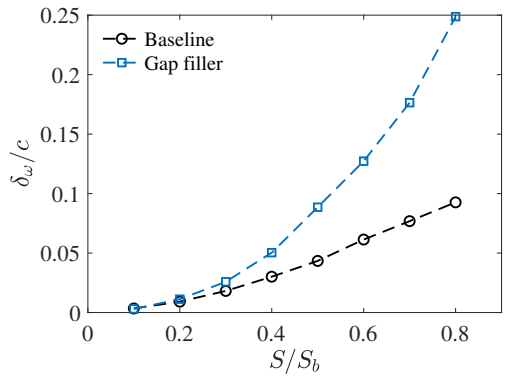


**Fig. 25 Nondimensional vorticity thickness for baseline and gap filler cases.**

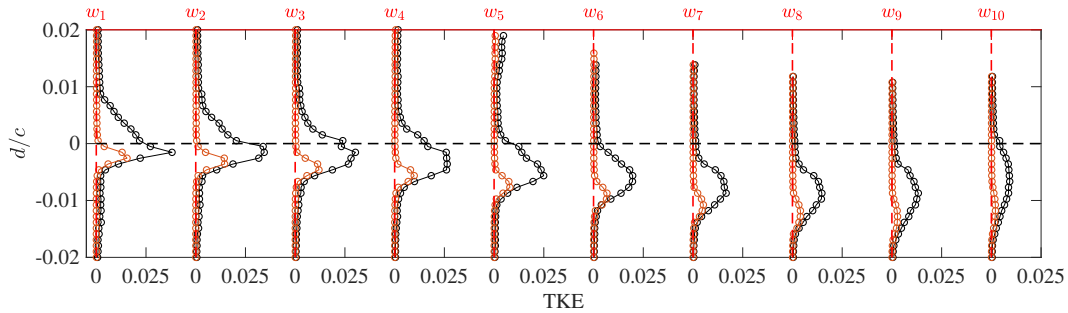


**(a) Slices of TKE**

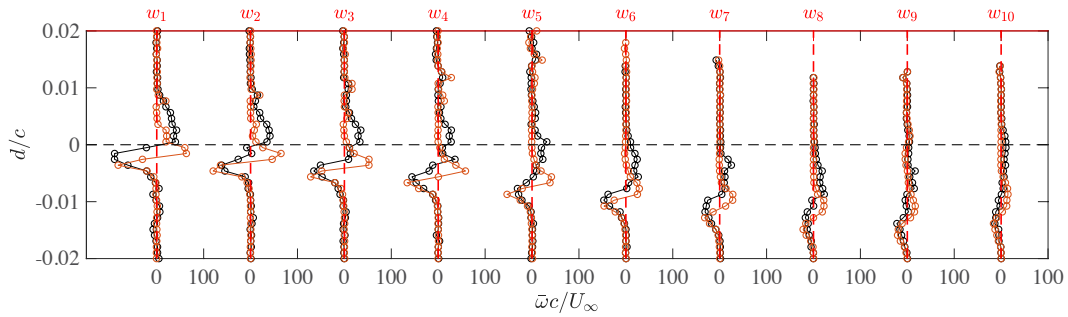


**(b) Slices of vorticity**

**Fig. 26 Slices of TKE and vorticity in the slat trailing edge shear layer. ○: baseline and ○: Cove filler.**

## IV. Conclusions

Two-dimensional PIV measurements are conducted on multiple passive noise treatment devices using an optical arrangement to observe both the suction and pressure sides simultaneously. The passive noise treatment devices include three slat extensions, a gap filler, and a cove filler, of which aerodynamic and noise control performance on a 2D 30P30N model were assessed in our previous work [19, 23]. The current experimental results elucidate the flow physics for reducing the slat noise, providing insights into the development and optimization of future slat noise control devices.

The slat extensions are found to shorten the slat-cove shear layer trajectory without changing the shear layer growth

rate. As the shear layer path is shortened, the disturbances in the shear layer have less time to grow. As a consequence, the longest slat extension achieved the highest level reduction in OASPL among the tested slat extensions [19]. The alteration of the shear layer results in the suppression of tonal peaks and the shift of tones to higher frequencies, as observed in our previous study. Based on the fluid-acoustic feedback hypothesis, the slat-cove shear layer length is selected as the length scale for Strouhal number. With this scaling, the nondimensional frequencies of the tonal peaks of far field acoustics for different slat extension cases measured in our previous study [19] collapse very well. The slat extensions also reduce the TKE levels but have negligible effects on the spanwise vorticity in the slat wake region. From local surface fluctuating pressure measurements near the slat trailing edge, the tonal peak due to the slat trailing edge vortex shedding was barely affected by different slat extensions [19].

The gap filler blocks the flow through the gap, and a straight slat-cove shear layer is formed. The straight slat-cove shear layer thus reattaches to the main wing lower surface, which breaks the acoustic feedback loop present in the baseline case. The newly established flow features lead to a more stable and widespread slat-cusp shear layer, with TKE levels approximately 50% those of the baseline case. This noise treatment device successfully reduced the OASPL far field noise level by almost 13 dB [23]. The accelerated flow and enlarged recirculation in the cove lead to increased lift on the slat portion, while lift is reduced on the main element due to the extensive flow separation on the suction side of the gap filler. Note that the aerodynamic penalty could be potentially resolved by making the gap filler porous or more streamlined. Combined with its excellent noise reduction performance, the gap filler is a valuable noise treatment candidate that should be optimized and investigated further.

In the cove filler case, the mean velocity components are highly similar to the baseline case except that the slat-cove shear layer is successfully eliminated as designed. As the slat-cove shear layer is absent, the tonal peaks due to the Kelvin-Helmholtz instability and acoustic feedback loop all disappear in the far field acoustics with a reduction of 14 dB in OASPL [19]. The cove filler also has an impact on the slat trailing edge vortex shedding in that the trailing edge shear layer is slightly deflected. In addition, the extent of the high vorticity region in the slat trailing edge shear layer is more confined, while the TKE levels are significantly reduced to half those of the baseline case. The more orderly shear layer leads to a sharper and higher level tonal peak in the previous surface fluctuating pressure measurements [19].

## Acknowledgments

The work reported here was performed under NASA Contract 80NSSC18P3447. The authors would like to thank Mr. Christopher Mark Cagle of the NASA Langley Research Center for his help with the hardware design of the slat brackets and all three noise reduction treatments; as well as the NASA Langley machine shop for fabricating the instrumented slat model and the treatments evaluated during the current work. Thanks are also due to the FSU machinists Robert Avant and Adam Piotrowski for hardware modifications.

## References

[1] Dobrzynski, W., "Almost 40 Years of Airframe Noise Research: What Did We Achieve?" *Journal of Aircraft*, Vol. 47, 2010, pp. 353–367.

[2] Zhang, X., *Airframe Noise: High Lift Device Noise*, John Wiley & Sons, Ltd, 2010. https://doi.org/10.1002/9780470686652.

[3] Terracol, M., Manoha, E., and Lemoine, B., "Investigation of the Unsteady Flow and Noise Generation in a Slat Cove," *AIAA Journal*, Vol. 54, No. 2, 2016, pp. 469–489. https://doi.org/10.2514/1.j053479.

[4] Pascioni, K. A., and Cattafesta, L. N., "Unsteady Characteristics of a Slat-Cove Flow Field," *Phys. Rev. Fluids*, Vol. 3, 2018. https://doi.org/10.1103/PhysRevFluids.3.034607.

[5] Rossiter, J. E., "Wind-tunnel Experiments on the Flow over Rectangular Cavities at Subsonic and Transonic Speeds," Tech. rep., Aeronautical Research Council Reports and Memoranda, 1964. No. 3438.

[6] Guo, Y., "Slat noise modeling and prediction," *Journal of Sound and Vibration*, Vol. 331, No. 15, 2012, pp. 3567–3586. https://doi.org/10.1016/j.jsv.2012.03.016.

[7] Choudhari, M. M., and Khorrami, M. R., "Effect of Three-Dimensional Shear-Layer Structures on Slat Cove Unsteadiness," *AIAA Journal*, Vol. 45, No. 9, 2007, pp. 2174–2186. https://doi.org/10.2514/1.24812.

[8] Knacke, T. J., and Thiele, F., "Numerical Analysis of Slat Noise Generation," *19th AIAA/CEAS Aeroacoustics Conference*, American Institute of Aeronautics and Astronautics, 2013. https://doi.org/10.2514/6.2013-2162, AIAA Paper 2013-2162.

[9] Khorrami, M. R., Berkman, M. E., and Choudhari, M., "Unsteady flow computations of a slat with a blunt trailing edge," *AIAA Journal*, Vol. 38, 2000, pp. 2050–2058. https://doi.org/10.2514/3.14649.

[10] Singer, B. A., Lockard, D. P., and Brentner, K. S., "Computational Aeroacoustic Analysis of Slat Trailing-Edge Flow," *AIAA Journal*, Vol. 38, No. 9, 2000, pp. 1558–1564. https://doi.org/10.2514/3.14581.

[11] Pascioni, K., "An Aeroacoustic Characterization of a Multi-Element High-Lift Airfoil," Ph.D. thesis, Florida State University, Tallahassee, FL, 2017.

[12] Choudhari, M., Lockard, D., Macaraeg, M., Singer, B., Streett, C., Neubert, G., Stoker, R., Underbrink, J., Berkman, M., Khorrami, M., and Sadowski, S., "Aeroacoustic Experiments in the Langley Low-Turbulence Pressure Tunnel," Tech. rep., NASA, 2002. TM 2002-211432.

[13] Streett, C., Casper, J., Lockard, D., Khorrami, M., Stoker, R., Elkoby, R., Wenneman, W., Underbrink, J., Wenneman, W., and Underbrink, J., "Aerodynamic Noise Reduction for High-Lift Devices on a Swept Wing Model," *44th AIAA Aerospace Sciences Meeting and Exhibit*, American Institute of Aeronautics and Astronautics, 2006. https://doi.org/10.2514/6.2006-212, AIAA Paper 2006-212.

[14] Imamura, T., Ura, H., Yokokawa, Y., Enomoto, S., Yamamoto, K., and Hirai, T., "Designing of Slat Cove Filler as a Noise Reduction Device for Leading-edge Slat," *13th AIAA/CEAS Aeroacoustics Conference (28th AIAA Aeroacoustics Conference)*, American Institute of Aeronautics and Astronautics, 2007. https://doi.org/10.2514/6.2007-3473, AIAA Paper 2007-3473.

[15] Jawahar, H. K., Theunissen, R., Azarpeyvand, M., and da Silva, C. R. I., "Flow characteristics of slat cove fillers," *Aerospace Science and Technology*, Vol. 100, 2020, p. 105789. https://doi.org/10.1016/j.ast.2020.105789.

[16] Scholten, W. D., Hartl, D. J., Turner, T. L., and Kidd, R. T., "Development and Analysis-Driven Optimization of Superelastic Slat-Cove Fillers for Airframe Noise Reduction," *AIAA Journal*, Vol. 54, No. 3, 2016, pp. 1078–1094. https://doi.org/10.2514/1.j054011.

[17] Bridges, J., and Brown, C., "Parametric Testing of Chevrons on Single Flow Hot Jets," *10th AIAA/CEAS Aeroacoustics Conference*, American Institute of Aeronautics and Astronautics, 2004. https://doi.org/10.2514/6.2004-2824, AIAA Paper 2004-2824.

[18] Kopiev, V., Zaitsev, M., Belyaev, I., and Mironov, M., "Noise Reduction Potential through Slat Hook Serrations," *17th AIAA/CEAS Aeroacoustics Conference (32nd AIAA Aeroacoustics Conference)*, American Institute of Aeronautics and Astronautics, 2011. https://doi.org/10.2514/6.2011-2909, AIAA Paper 2011-2909.

[19] Zhang, Y., O'Neill, A., Cattafesta, L. N., Pascioni, K., Choudhari, M., Khorrami, M. R., Lockard, D. P., and Turner, T., "Assessment of Noise Reduction Concepts for Leading-Edge Slat Noise," *2018 AIAA/CEAS Aeroacoustics Conference*, American Institute of Aeronautics and Astronautics, 2018. https://doi.org/10.2514/6.2018-3461, AIAA Paper 2018-3461.

[20] Pagani, C. C., Souza, D. S., and Medeiros, M. A., "Experimental investigation on the effect of slat geometrical configurations on aerodynamic noise," *Journal of Sound and Vibration*, Vol. 394, 2017, pp. 256–279. https://doi.org/10.1016/j.jsv.2017.01.013.

[21] Turner, T. L., Khorrami, M. R., Lockard, D. P., McKenney, M. J., Atherley, R. D., and Kidd, R. T., "Multi-Element Airfoil System," , July 2014. US Patent 8763958.

[22] Turner, T. L., and Long, D. L., "Development of a SMA-Based, Slat-Gap Filler for Airframe Noise Reduction," *23rd AIAA/AHS Adaptive Structures Conference*, American Institute of Aeronautics and Astronautics, 2015. https://doi.org/10.2514/6.2015-0730, AIAA Paper 2015-0730.

[23] Zhang, Y., Cattafesta, L. N., Pascioni, K. A., Choudhari, M. M., Lockard, D. P., Khorrami, M. R., and Turner, T., "Slat Noise Control Using a Slat Gap Filler," *AIAA AVIATION 2020 FORUM*, American Institute of Aeronautics and Astronautics, 2020. https://doi.org/10.2514/6.2020-2553, AIAA Paper 2020-2553.

[24] Westerweel, J., and Scarano, F., "Universal Outlier Detection for PIV Data," *Experiments in Fluids*, Vol. 39, No. 6, 2005, pp. 1096–1100. https://doi.org/10.1007/s00348-005-0016-6.

[25] Griffin, J., Schultz, T., Holman, R., Ukeiley, L. S., and Cattafesta, L. N., "Application of multivariate outlier detection to fluid velocity measurements," *Experiments in Fluids*, Vol. 49, No. 1, 2010, pp. 305–317. https://doi.org/10.1007/s00348-010-0875-3.

[26] Pascioni, K. A., and Cattafesta, L. N., "An aeroacoustic study of a leading-edge slat: Beamforming and far field estimation using near field quantities," *Journal of Sound and Vibration*, Vol. 429, 2018, pp. 224–244. https://doi.org/10.1016/j.jsv.2018.05.029.

[27] Mu, M. S., Schrass, J., Lieb, K. F., and Hartl, D. J., "Aerodynamic and Aeroacoustic Experimentation of a Slat-Gap Filler for Airframe Noise Reduction," *AIAA Scitech 2021 Forum*, American Institute of Aeronautics and Astronautics, 2021. https://doi.org/10.2514/6.2021-1997, AIAA Paper 2021-1997.

[28] Jawahar, H. K., Azarpeyvand, M., and Silva, C., "Numerical Investigation of High-lift Airfoil Fitted with Slat Cove Filler," *25th AIAA/CEAS Aeroacoustics Conference*, American Institute of Aeronautics and Astronautics, 2019. https://doi.org/10.2514/6.2019-2439, AIAA Paper 2019-2439.

[29] Kerschen, E., and Tumin, A., "A Theoretical Model of Cavity Acoustic Resonances Based on Edge Scattering Processes," *41st Aerospace Sciences Meeting and Exhibit*, American Institute of Aeronautics and Astronautics, 2003. https://doi.org/10.2514/6.2003-175, AIAA Paper 2003-175.

[30] Rowley, C. W., Williams, D. R., Colonius, T., Murray, R. M., and Macmynowski, D. G., "Linear models for control of cavity flow oscillations," *Journal of Fluid Mechanics*, Vol. 547, 2006, pp. 317–330. https://doi.org/10.1017/s0022112005007299.